Multiconfigurational calculations and photodynamics describe norbornadiene photochemistry

Federico J. Hernández,[b] Jordan M. Cox,[a] and Jingbai Li,*[,c] Rachel Crespo-Otero,[b,*] and Steven A. Lopez[a,*]

[a] Department of Chemistry and Chemical Biology, Northeastern University, Boston, MA 02115, U.S.A.
[b] School of Physical and Chemical Sciences, Queen Mary University of London, Mile End Road, London E1 4NS, U.K.
[c] Hoffmann Institute of Advanced Materials, Shenzhen Polytechnic, 7098 Liuxian Blvd, Nanshan District, Shenzhen, 518055, People's Republic of China

* Correspondence to lijingbai@szpt.edu.cn, r.crespo-otero@qmul.ac.uk and s.lopez@northeastern.edu

Abstract
Storing solar energy is a vital component of using renewable energy sources to meet the growing demands of the global energy economy. Molecular solar thermal (MOST) energy storage is a promising means to store solar energy with on-demand energy release. The light-induced isomerization reaction of norbornadiene (NBD) to quadricyclane (QC) is of great interest because of the generally high energy storage density (0.97 $MJ \cdot kg^{-1}$) and long thermal reversion lifetime ($t_{1/2,\ 300K}$ = 8346 years). However, the mechanistic details of the ultrafast excited-state [2+2]-cycloaddition is largely unknown due to the limitations of experimental techniques in resolving accurate excited-state molecular structures. We now present a full computational study on the excited-state deactivation mechanism of NBD in the gas phase. Our multiconfigurational calculations [SA6-CASSCF(4,7)/ANO-S-VDZP] and non-adiabatic molecular dynamics simulations have enumerated the possible pathways with 600 S_2 initial conditions for 300 fs. The predicted S_2 and S_1 lifetimes are reported (62 and 221 fs). The QC: NBD formation ratio is 1:5; the predicted quantum yield of QC is 9%, which underscores the potential of NBD for MOST materials. Our simulations also show the mechanisms of forming other possible reaction products and their quantum yields.

1. Introduction

Sunlight is an essentially renewable and sustainable energy resource. The utilization of solar energy requires effective technologies to convert intermittent sunlight into steady electricity or fuel for regular usage. Efforts have been made to develop, for instance, solar cells,[1-6] CO_2 reductions,[7-10] water splitting,[11, 12] energy-dense fuels,[13, 14] photoswitches,[15-17] and solar thermal storage.[18] Among various prominent technologies, molecular solar thermal (MOST) energy storage provides a promising tool to store solar energy and release it on demand.[19-21] MOST devices are developed based on photoswitchable molecules. MOST materials isomerize from a thermodynamically stable structure to a metastable structure, storing the absorbed energy in strained chemical bonds. Many organic molecules have been investigated for MOST applications, such as azobenzene,[16,

[22-24] anthracene,[25, 26] tetracarbonyl-fulvalene-diruthenium,[27-30] dihydroazulene/vinylheptafulvene (DHA/VHF),[31-34] bicyclooctadiene/tetracyclooctane (BOD/TCO)[35, 36] and norbornadiene/quadricyclane (NBD/QC).[37-43] The NBD/QC system is one of the top candidates, where the NBD undergoes a [2+2]-photocycloaddition to the photoisomer QC (Figure 1).[44, 45]

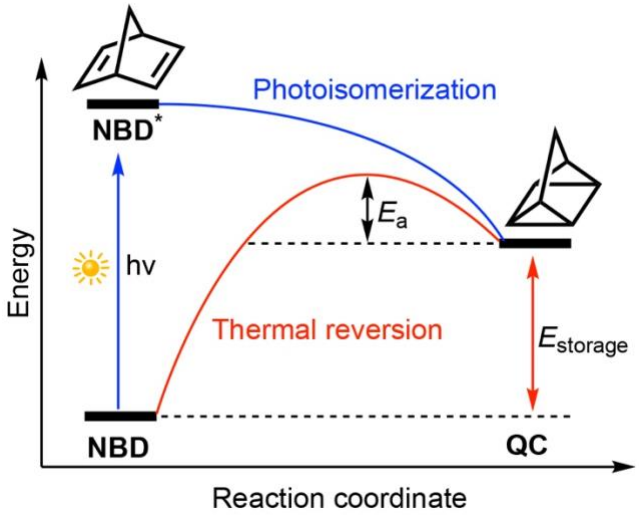

Figure 1. Illustration of solar thermal energy storage based on NBD and QC isomerization.

The thermal reversion of QC to NBD releases storage energy of 88 kJ·mol^{-1}, corresponding to a storage density of 0.97 MJ·kg^{-1}.[35] The back reaction barrier of QC is about 138 kJ·mol^{-1},[46] which leads to a half-life of 14 hours at 140 °C (i.e., $t_{1/2,\ 300K}$ = 8,346 years).[47] Such a lifetime allows the NBD/QC system to store the accumulated solar energy effectively. However, the high energy of absorption maximum (200–230 nm[48, 49]) and the modest quantum yield (QY) of QC (5%) could limit its efficiency for solar energy conversion.[20, 41, 42, 50] Many studies have shown that the functionalization of the $\pi_{C\text{-}C}$ bonds of NBD can red-shift the absorption and increase the QY.[37, 39, 40, 51-54] But the increased molecular weight of substituents reduces the energy storage density to 0.10–0.56 MJ·kg^{-1}.[41] A high-throughput virtual screening studies on 3239 NBDs[55] and screening and another machine-learning-assisted screening of over 10^{25} substituted NBD discovered only 15 candidates with absorption longer than 350 nm, storage density larger than 0.4 MJ·kg^{-1}, and back reaction barriers exceeding 150 kJ·mol^{-1} ($t_{1/2,\ 300K}$ = 459824 years).[56]

Literature reports on the photophysical properties and reaction energies provide important design features but considerably less is known about the excited-state reaction mechanisms of NBD and its derivatives. The ultrafast photochemical NBD→QC interconversion has been the primary focus of computational and experimental elucidation of the low-lying absorption at 212 nm (5.85 eV) corresponding to excitation to the 3s Rydberg state.[49, 57, 58] The mechanistic studies are limited to the exploration of the excited-state potential energy surface and characterization of the S_1/S_0 minimum energy conical intersection (MECI).[59] The S_1/S_0 MECI shows a bond-forming geometry indicating an important role in the [2+2]-cycloaddition reactions. A grid-based quantum dynamics study of NBD observed $S_1 \rightarrow S_0$ transition through the S_1/S_0 MECI, while the simulations were carried out in only 3 degrees of freedom.[60] Other reports described the substituent effects on the excitation energy, excited-state minimum energy path, and the energy storage of the functionalized NBD systems.[61, 62] However, the excited-state dynamics of NBD that fully traverse

the reaction coordinate from the initially excited NBD (Franck-Condon region) to product(s) have not been explored yet. In this work, we use nonadiabatic dynamics coupled with CASSCF calculations to study the deactivation pathways of photoexcited NBD. We analyze the deactivation mechanism after photoexcitation. We also offer a complete mechanistic map showing all possible reaction products and their predicted quantum yields.

2. Computational methods

We selected the CASSCF method for the gas-phase excitations and prepared a suitable active space. Previous experimental and theoretical studies found a low-lying absorption at 212 nm (5.85 eV) corresponding to an excitation to the 3s Rydberg state.[49, 57, 58] Antol proposed a (4,5) active space of 4 π-electrons and 4 π-orbitals with restricted single excitations to an auxiliary 3s-orbital to compute the excited-state potential energy surface (PES) of NBD.[59] Recently, Remacle and co-workers included another 3p-orbital forming an (8,8) space to model the quantum dynamics of NBD over the 8 electronic states.[60] Since we are interested in the photochemical reactions of NBD occurring in the low-lying states, we considered a (4,7) active space with 3s-, $3p_x$-, and $3p_y$-orbitals. The selection of these Rydberg orbitals was based on the lowest 4 excitations. We benchmarked the excitations of NBD with time-dependent functional theory (TD-DFT) using the range-separated functional, ωB97XD[63] and equation of motion coupled cluster with singles and doubles (EOM-CCSD)[64] and the aug-cc-pVDZ basis sets (Table S1).[65] Figure 2 illustrates the (4,7) active space computed with 6 state averaged (SA6) CASSCF(4,7)/ANO-S-VDZP method. The ANO-S-VDZP basis set[66-69] has a quality generally comparable to aug-cc-pVDZ.[70]

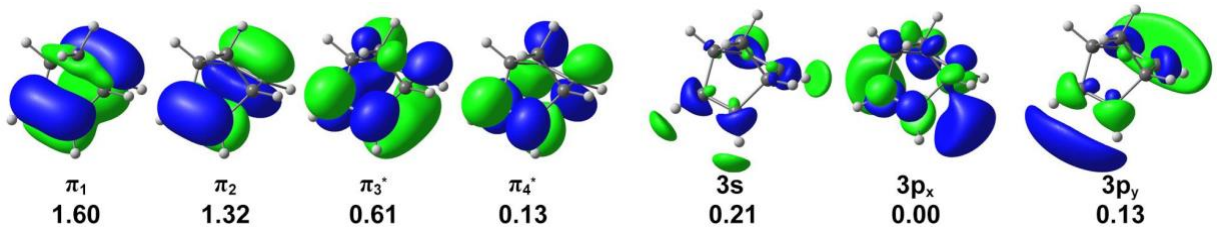

Figure 2. Illustration of the (4,7) space of NBD with the occupations averaged over six electronic states, computed with SA6-CASSCF(4,7)/ANO-S-VDZP. Isovalue is 0.03.

The geometries of NBD were optimized with SA6-CASSCF(4,7)/ANO-S-VDZP. A Hessian calculation confirmed a local minimum with no imaginary frequencies. We assessed the quality of CASSCF excitation energies with the extended multistate complete active space second-order perturbation (XMS-CASPT2) method due to the lack of dynamical electron corrections. For the SA6-CASSCF(4,7)/ANO-S-VDZP and XMS(6)-CASPT2(4,7)/ANO-S-VDZP calculations, we used OpenMolcas 19.11.[71] The TD-DFT and EOM-CCSD calculations were performed with ORCA 4.2.0.[72]

We combined the nonadiabatic molecular dynamics (NAMD) codes from PyRAI^{2}MD[73] with SA6-CASSCF(4,7)/ANO-S-VDZP from OpenMolcas to perform gas-phase NAMD simulations on NBD. The surface hopping calculations employed Tully's original formula based on the product of the time-independent nonadiabatic couplings (NACs) and velocities.[74, 75] Due to the arbitrary phase of NACs in CASSCF calculations, we applied phase corrections at every timestep based on the

NAC overlaps between two consecutive time steps.[76] To accelerate the simulations, we only considered the NACs between adjacent states and assumed zero coupling between nonadjacent states (e.g., states 1 and 3). The microcanonical ensemble (NVE) was considered in 300 fs of total simulation time with a timestep of 0.5 fs. We excluded the trajectories with unsatisfied total energy conservation. The fewest-switches surface hopping calculations integrated the nuclear amplitude with a step size of 0.02 fs (i.e., 25 substeps). We applied an energy-based decoherence correction of 0.1 Hartree to the nuclear amplitude.[77] At every event of surface hopping, the momenta were rescaled isotropically to ensure energy conservation.

800 initial conditions of NBD molecules were sampled for gas-phase NAMD simulations using the Wigner sampling at the zero-point energy level.[78, 79] The final number of trajectories was determined by ensuring the converged predictions of QYs were higher than the corresponding margin of error for a proportion in a 95% confidential interval (Figure S4). We also computed the vertical excitation energies of the Winger-sampled initial conditions of NBD to simulate the gas-phase absorption spectrum. The computed wavelengths were expanded with narrow Gaussian functions (i.e., full width at half maximum of 8 nm) and scaled with the oscillator strengths.

3. Results and discussion

We computed the gas-phase vertical excitation energies of 800 Wigner-sampled NBD structures to explore the nature of electronic excitations to the FC regions. We selected the SA6-CASSCF(4,7)/ANO-S-VDZP method after a careful benchmark comparing with other methods of higher hierarchy and the available experimental values (see Section S1 in the Supporting Information). Figure 4 illustrates a convoluted spectrum with contributions from various excited-state electronic configurations.

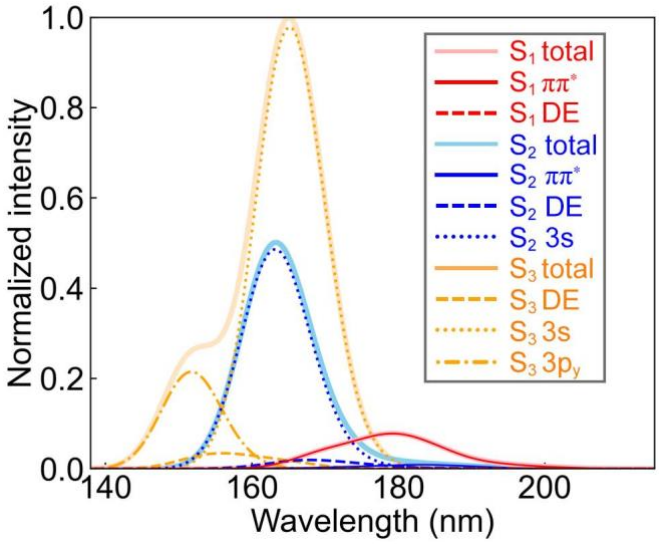

Figure 3. The simulated absorption spectrum for the first three bands. 800 NBD non-equilibrium structures used to compute vertical excitation energies with SA6-CASSCF(4,7)/ANO-S-VDZP. The absorption bands are decomposed according to their excited-state electronic configurations (DE means doubly excited).

The SA6-CASSCF(4,7)/ANO-S-VDZP calculations predict a broad S_1 absorption peak in 160–200 nm, centered at 180 nm, in line with the experimental report by Fuß *et al*.[49] S_1 is dominated by a $\pi\pi^*$ state (94%) mixed with a minor doubly excited (DE) state (6%). The computed intensity of absorption to S_1 is non-zero, suggesting that the $\pi\pi^*$ state is accessible from the non-equilibrium NBD geometries. The S_2 and S_3 peaks overlap at 150–180 nm. They show strong absorption intensities corresponding to the 3s-Rydberg state. The 3s-Rydberg state in S_2 is 40%, and the competing DE and $\pi\pi^*$ states are 46% and 14%, respectively. However, the DE and $\pi\pi^*$ intensities are considerably lower than the 3s-Rydberg state (Figure 3). S_3 is comprised of 3s-Rydberg state (60%), DE state (27%), and $3p_y$-Rydberg state (12%). The $3p_y$-Rydberg state leads to a shoulder at 150 nm. The simulated spectrum for S_2 qualitatively agrees with the experiments by Fuß and co-workers, where the irradiation populates both the 3s-Rydberg and the $\pi\pi^*$ states.[49]

We performed minimum energy path (MEP) calculations to explore the steepest descent pathways from the (Franck-Condon) FC points of NBD and establish a pseudo-dominant path toward mechanistic critical points (e.g., minimum energy conical intersection). Following the S_3 and S_2 states, the MEPs quickly converged on an excited-state local minimum (Figures S1 and S2). In contrast, the MEP from the S_1-FC point provides an informative description of the nonradiative [2+2]-cycloaddition pathway of NBD toward QC. Figure 4a and 4b compare the S_1 MEP optimized with the SA6-CASSCF(4,7)/ANO-S-VDZP method and those corrected with XMS(6)-CASPT2(4,7)/ANO-S-VDZP.

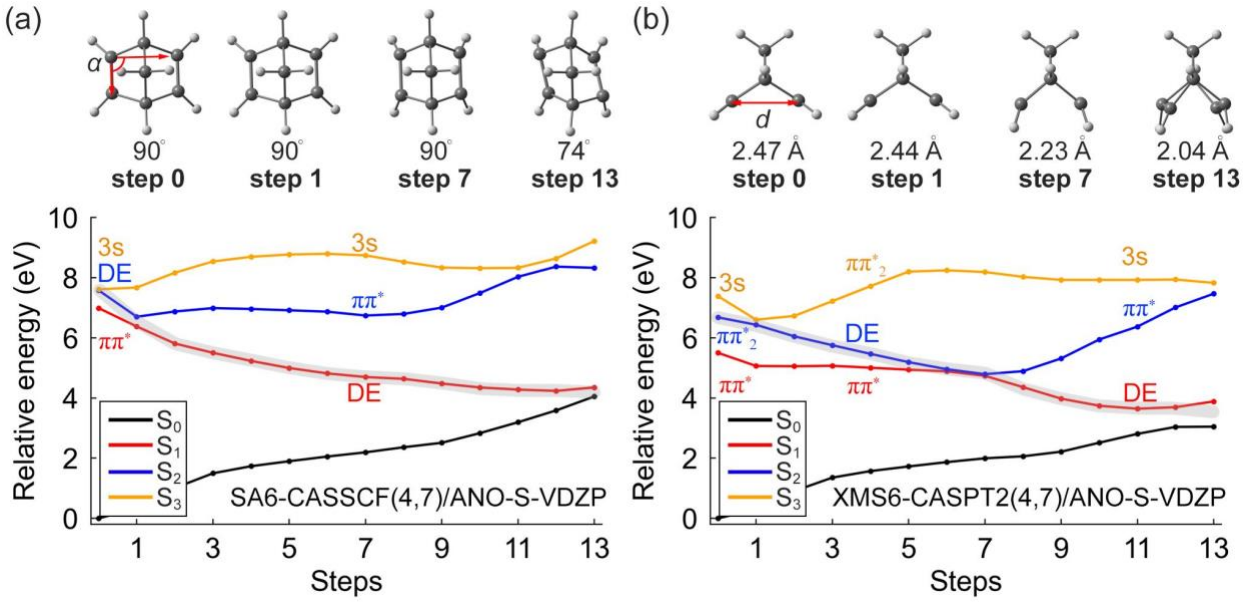

Figure 4. Minimum energy paths of NBD optimized with the SA6-CASSCF(4,7)/ANO-S-VDZP (a) and corrected with the XMS(6)-CASPT2(4,7)/ANO-S-VDZP (b). The minimization path follows the S_1 toward the S_1/S_0 MECI. The gray curves highlight possible S_2 relaxation pathways.

We identified two parameters to quantify the structural changes along the reaction coordinate: a rhomboidal angle among the bond-forming carbon, α, and a distance between the $\pi_{C\text{-}C}$ bonds, d (Figure S3). At the S_1-FC region, d and α are 2.47 Å and 90°, respectively. Figure 4a shows that

the MEP along the S_1 slightly decreases the $\pi_{C\text{-}C}$-distance (Δd = 0.03Å) at step 1, which switches the state-order between the $\pi\pi^*$ and the DE states. In the following steps, the DE state dominates the S_1 state. The geometrical parameters resemble a rhomboidal shape (α = 74° and d = 2.04 Å), consistent with the previously reported S_1/S_0-MECI structures by Antol.[59] The XMS(6)-CASPT2(4,7)/ANO-S-VDZP MEP suggests the $\pi\pi^*$ and DE states are separated by the 3s-Rydberg and $\pi\pi^*_2$ states at the S_1-FC geometry (Figure 4b). The DE state appears in S_2 at the first step as the energy decreases with the $\pi_{C\text{-}C}$-distance. The DE state then leads to an S_2/S_1 crossing point at step 7 with d = 2.23 Å (Figure 4b). This indicates that the SA6-CASSCF(4,7)/ANO-S-VDZP overestimates the $\pi_{C\text{-}C}$-distance at the S_2/S_1 crossing point. Nevertheless, the SA6-CASSCF(4,7)/ANO-S-VDZP and XMS(6)-CASPT2(4,7)/ANO-S-VDZP results agree that the DE state in S_2 drives the excited-state PES to the S_1**/**S_0 crossing point for the [2+2]-cycloaddition of NBD.

The excitation energies to the S_2 and S_3 states are nearly degenerate (Table S1), and their electronic excitations are mixtures of 3s-Rydberg and DE states (Figure 3). We, therefore, expect the NBD trajectories starting from S_3 would undergo rapid internal conversion to S_2 with negligible structural changes. Hence, we started 300 fs gas-phase NAMD simulations from S_2. We propagated 645 trajectories to obtain statistically converged results (Figures 5 and S4).

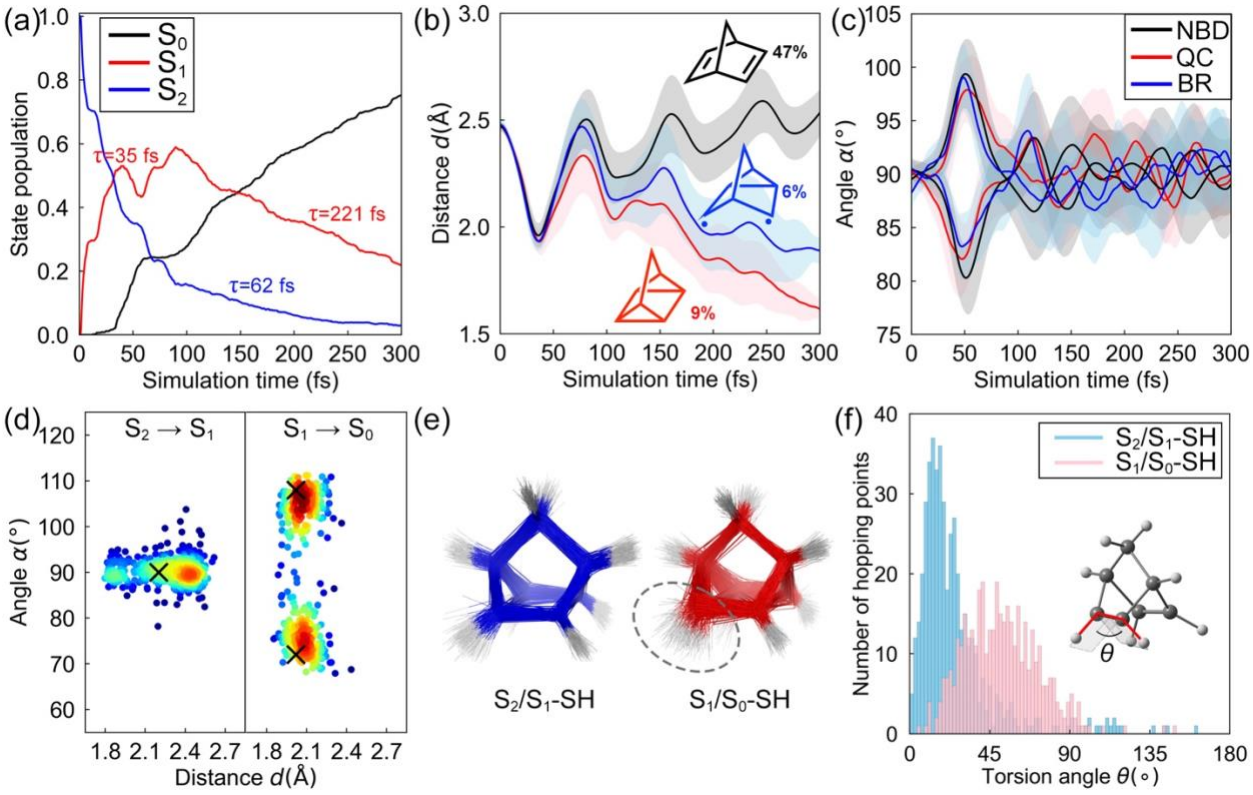

Figure 5. State population (a), average $\pi_{C\text{-}C}$-distance (b), rhomboidal angle (c), and surface hopping distributions (d) of 645 NBD trajectories in the gas phase. In panels (b) and (c), the shaded regions render a half standard deviation to the average values to show the diversity of the trajectories. In panel (d), the "X" denotes the positions of the S_2/S_1 and S_1/S_0 MECIs. The colors from blue to red represent the accumulation of the surface hopping points from low to high,

evaluated by Gaussian kernel density estimation. (e) Overlays of the 200 randomly selected S_2/S_1 and S_1/S_0 surface hopping structures. The gray circle highlights the pyramidalization of the $\pi_{C\text{-}C}$ bond in the S_1/S_0 surface hopping structures. (f) Distributions of the torsion angle θ among the S_2/S_1 and S_1/S_0 surface hopping structures. The θ values in the S_2/S_1 and S_1/S_0-MECI are 0° and 32° respectively.

After 300 fs, 75% of the trajectories were in the S_0 state, 22% and 3% remained in S_1 and S_2, respectively. Figure 5a illustrates an exponential decay of the S_2 population with a time constant τ = 62 fs. The trajectories excited to the 3s-Rydberg state show τ = 67 fs (Figure S5). The S_1 ($\pi\pi^*$ state) population increases to 0.53 after 40 fs (τ = 35 fs) and approaches a local minimum of 0.43 at 58 fs; the population rises to the second maximum of 0.59 at 90 fs. The overall $S_1 \rightarrow S_0$ decay leads to τ = 221 fs. The previous experiment by Fuß and co-workers measured a longer time constant of the 3s-Rydberg state (τ = 420 fs) than the $\pi\pi^*$ state (τ = 55 fs).[49] However, our results suggest that the lifetime of the 3s-Rydberg state (τ = 67 fs) is shorter than the $\pi\pi^*$ state (τ = 221 fs). This difference may result from a local overestimation of the S_1-PES energy near the FC region with SA6-CASSCF(4,7)/ANO-S-VDZP (compare Figures 4a and 4b). Such energy overestimation decreases the S_2-S_1 energy gap, thus accelerating the $S_2 \rightarrow S_1$ decay from the 3s-Rydberg state and causing a slower $S_1 \rightarrow S_0$ decay.

Figures 5b and 5c illustrate substantial structural changes of NBD during the 300 fs simulations. Structural parameters d and α have average values of 2.47 Å and 90° at the start of the trajectories. All trajectories instantaneously reduce the $\pi_{C\text{-}C}$-distances below 2 Å within 50 fs (Figure 5b). At the same time, the rhomboidal angles undergo substantial oscillations at 80–100° (Figure 5c). The trajectories then split into three pathways, 1) reversion to NBD (47%), 2) formation of the QC product (9%), and 3) formation of a singlet biradical (BR) intermediate (6%). The predicted QY of QC (9%) is in reasonable agreement with the experimental QY (5%).[20, 41, 42, 50.] It also suggests a QC: NBD formation ratio of 1: 5.

The structural changes of NBD originate from the non-radiative decay through the S_2/S_1 and subsequent S_1/S_0 crossing seams. Figure 5d shows a scatter plot of the 3D geometries of the hopping points projected onto two reaction coordinates (d and α). The majority of the S_2/S_1 hopping points (centered at d = 2.44 Å) are structurally related to those in the S_2-FC region (centered at d = 2.47 Å). In contrast, a minority of those trajectories passing through the S_2/S_1 surface hopping points access the S_2/S_1-MECI (d = 2.20 Å and α = 90°) region. We interpret that the rapid $S_2 \rightarrow S_1$ decay (Figure 5a) arises from the geometric proximity of the structures in the S_2-FC region and S_2/S_1 crossing seam. The S_1/S_0 surface hopping is concentrated near d = 2.06 Å with a symmetric angular distribution at α = 74° and 102° (Figure 5d). The symmetric angular distribution indicates two equivalent S_1/S_0 crossing seams around the S_1/S_0-MECI at d = 2.02 Å and α = 72° (108°). Figure 5e shows an overlay of the S_2/S_1 and S_1/S_0 hopping points. The S_2/S_1 surface hopping structures resemble a midpoint of the linear interpolated structures between NBD and QC. However, most S_1/S_0 surface hopping structures feature a pyramidalized $\pi_{C\text{-}C}$ bond. We quantify the extent of the pyramidalization with an HCCH torsion angle, θ. Figure 5f illustrates a histogram of θ in the trajectories to describe the $\pi_{C\text{-}C}$-pyramidalization distribution at the S_1/S_0 crossing seam. The θ ranges from 0–160° at the S_2/S_1 hopping points, but the average value is 26°. In the S_1/S_0 hopping points, θ ranges from 0–149°, and the average value increases to 52°. These results agree with prior assertions that $\pi_{C\text{-}C}$ pyramidalization affords easier access to

chemically productive S_1/S_0 conical intersections. Similar phenomena have been reported in the conical intersection and surface hopping structures of photoexcited conjugated molecules.[73, 80, 81].

Besides the major products, our NAMD simulations also identified several side reaction rearrangement pathways (Figure 6).

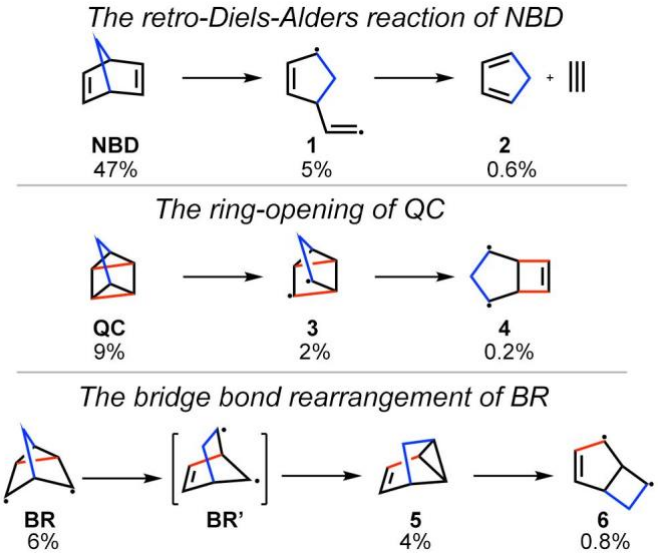

Figure 6. Side-reactions observed in the gas-phase NBD trajectories with the ratios of products or intermediates. The methylene bridge and the newly formed $\sigma_{C\text{-}C}$-bonds in QC are highlighted in blue and red, respectively. The proposed intermediate BR' converts BR to **3** according to the NBD trajectories.

These reactions feature breaking $\sigma_{C\text{-}C}$-bonds; the CASSCF rotates the $\sigma_{C\text{-}C}$-orbitals into the (4,7) active space as the $\sigma_{C\text{-}C}$-bonds stretch beyond their equilibrium geometries during the trajectories. The QYs for the ring-opening and rearrangement pathways are relatively minor (0.2–5%) compared to the reversion of NBD (47%) and [2+2]-cycloaddition pathways (9%). Nevertheless, the predicted side reactions suggest a qualitative agreement with the photodegradation of substituted NBD observed in experiments.[82] Future studies will explore substituent effects to change the photophysical properties and optimize the QY and chemical yields of QC by blocking the competing rearrangement and retro-[4+2] cycloadditions.

4. Conclusions

We have used CASSCF calculations combined with nonadiabatic dynamics to elucidate the deactivation mechanisms for photoexcited NBD. The vertical excitation energies reveal the significant role of Rydberg states in the absorption of NBD, in line with previous experimental and computational studies. We performed 645 NAMD simulations for 300 fs, effectively connecting the FC region to the product region and identifyied products beyond QC propagated from the bright S_2 state. Besides forming the rhomboidal structures at the S_1/S_0 surface hopping points, we also observed the pyramidalization of the $\pi_{C\text{-}C}$ bonds, facilitating the non-radiative decay. The predicted gas-phase QYs of NBD, QC, and BR are 47%, 9%, and 6%, respectively. Future studies will focus on crystalline phase photochemistry on substituted NBDs that are crystalline above room temperature.

Acknowledgments
J.L. and S.A.L. acknowledge the National Science Foundation CAREER award (NSF-CHE-2144556). J.L. and S.A.L. appreciate the assistance from the Northeastern Research Computing Team and the computing resources provided by the Massachusetts Life Science Center grant (G00006360). F.J.H. and R.C.O. acknowledge the funding by the Leverhulme Trust (RPG-2019-122) and the MMM Hub, partially funded by EPSRC(EP/T022213/1) and QMUL Research-IT for access to computational resources. F.J.H., R.C.O., and S.A.L. acknowledge the Royal Society for funding through an International Exchange grant (IES\R2\222057).

Supporting information
Cartesian coordinates of optimized structures, electronic energies, excitation energy benchmarks, and additional information on NBD trajectories.

Reference
(1) Carey, G. H.; Abdelhady, A. L.; Ning, Z.; Thon, S. M.; Bakr, O. M.; Sargent, E. H. Colloidal Quantum Dot Solar Cells. *Chem. Rev.* **2015**, *115* (23), 12732-12763. DOI: 10.1021/acs.chemrev.5b00063.
(2) Lu, L.; Zheng, T.; Wu, Q.; Schneider, A. M.; Zhao, D.; Yu, L. Recent Advances in Bulk Heterojunction Polymer Solar Cells. *Chem. Rev.* **2015**, *115* (23), 12666-12731. DOI: 10.1021/acs.chemrev.5b00098.
(3) Kim, J. Y.; Lee, J. W.; Jung, H. S.; Shin, H.; Park, N. G. High-Efficiency Perovskite Solar Cells. *Chem. Rev.* **2020**, *120* (15), 7867-7918. DOI: 10.1021/acs.chemrev.0c00107.
(4) Peng, W.; Rupich, S. M.; Shafiq, N.; Gartstein, Y. N.; Malko, A. V.; Chabal, Y. J. Silicon Surface Modification and Characterization for Emergent Photovoltaic Applications Based on Energy Transfer. *Chem. Rev.* **2015**, *115* (23), 12764-12796. DOI: 10.1021/acs.chemrev.5b00085.
(5) Nayak, P. K.; Mahesh, S.; Snaith, H. J.; Cahen, D. Photovoltaic solar cell technologies: analysing the state of the art. *Nature Reviews Materials* **2019**, *4* (4), 269-285. DOI: 10.1038/s41578-019-0097-0.
(6) Cox, J. M.; Mileson, B.; Sadagopan, A.; Lopez, S. A. Molecular Recognition and Band Alignment in 3D Covalent Organic Frameworks for Cocrystalline Organic Photovoltaics. *J. Phys. Chem. C* **2020**, *124* (17), 9126-9133. DOI: 10.1021/acs.jpcc.0c00087.
(7) Wang, W. H.; Himeda, Y.; Muckerman, J. T.; Manbeck, G. F.; Fujita, E. CO2 Hydrogenation to Formate and Methanol as an Alternative to Photo- and Electrochemical CO2 Reduction. *Chem. Rev.* **2015**, *115* (23), 12936-12973. DOI: 10.1021/acs.chemrev.5b00197.
(8) White, J. L.; Baruch, M. F.; Pander Iii, J. E.; Hu, Y.; Fortmeyer, I. C.; Park, J. E.; Zhang, T.; Liao, K.; Gu, J.; Yan, Y.; et al. Light-Driven Heterogeneous Reduction of Carbon Dioxide: Photocatalysts and Photoelectrodes. *Chem. Rev.* **2015**, *115* (23), 12888-12935. DOI: 10.1021/acs.chemrev.5b00370.
(9) Morikawa, T.; Sato, S.; Sekizawa, K.; Suzuki, T. M.; Arai, T. Solar-Driven CO2 Reduction Using a Semiconductor/Molecule Hybrid Photosystem: From Photocatalysts to a Monolithic Artificial Leaf. *Acc Chem Res* **2022**, *55* (7), 933-943. DOI: 10.1021/acs.accounts.1c00564.
(10) Nakada, A.; Kumagai, H.; Robert, M.; Ishitani, O.; Maeda, K. Molecule/Semiconductor Hybrid Materials for Visible-Light CO2 Reduction: Design Principles and Interfacial Engineering. *Acc. Mater. Res.* **2021**, *2* (6), 458-470. DOI: 10.1021/accountsmr.1c00060.
(11) Kang, D.; Kim, T. W.; Kubota, S. R.; Cardiel, A. C.; Cha, H. G.; Choi, K. S. Electrochemical Synthesis of Photoelectrodes and Catalysts for Use in Solar Water Splitting. *Chem. Rev.* **2015**, *115* (23), 12839-12887. DOI: 10.1021/acs.chemrev.5b00498.

(12) Wang, Q.; Domen, K. Particulate Photocatalysts for Light-Driven Water Splitting: Mechanisms, Challenges, and Design Strategies. *Chem. Rev.* **2020**, *120* (2), 919-985. DOI: 10.1021/acs.chemrev.9b00201.
(13) Liu, Y.; Chen, Y.; Ma, S.; Liu, X.; Zhang, X.; Zou, J.-J.; Pan, L. Synthesis of advanced fuel with density higher than 1 g/mL by photoinduced [2 + 2] cycloaddition of norbornene. *Fuel* **2022**, *318*. DOI: 10.1016/j.fuel.2022.123629.
(14) Xie, J.; Zhang, X.; Shi, C.; Pan, L.; Hou, F.; Nie, G.; Xie, J.; Liu, Q.; Zou, J.-J. Self-photosensitized [2 + 2] cycloaddition for synthesis of high-energy-density fuels. *Sustainable Energy & Fuels* **2020**, *4* (2), 911-920. DOI: 10.1039/c9se00863b.
(15) Calbo, J.; Weston, C. E.; White, A. J.; Rzepa, H. S.; Contreras-Garcia, J.; Fuchter, M. J. Tuning Azoheteroarene Photoswitch Performance through Heteroaryl Design. *J. Am. Chem. Soc.* **2017**, *139* (3), 1261-1274. DOI: 10.1021/jacs.6b11626.
(16) Gonzalez, A.; Kengmana, E. S.; Fonseca, M. V.; Han, G. G. D. Solid-state photoswitching molecules: structural design for isomerization in a condensed phase. *Mater. Today Adv.* **2020**, *6*. DOI: 10.1016/j.mtadv.2020.100058.
(17) Sun, C. L.; Wang, C.; Boulatov, R. Applications of Photoswitches in the Storage of Solar Energy. *ChemPhotoChem* **2019**, *3* (6), 268-283. DOI: 10.1002/cptc.201900030.
(18) Saydjari, A. K.; Weis, P.; Wu, S. Spanning the Solar Spectrum: Azopolymer Solar Thermal Fuels for Simultaneous UV and Visible Light Storage. *Adv. Energy Mater.* **2017**, *7* (3). DOI: 10.1002/aenm.201601622.
(19) Xu, X.; Wang, G. Molecular Solar Thermal Systems towards Phase Change and Visible Light Photon Energy Storage. *Small* **2022**, *18* (16), e2107473. DOI: 10.1002/smll.202107473.
(20) Wang, Z.; Erhart, P.; Li, T.; Zhang, Z.-Y.; Sampedro, D.; Hu, Z.; Wegner, H. A.; Brummel, O.; Libuda, J.; Nielsen, M. B.; et al. Storing energy with molecular photoisomers. *Joule* **2021**, *5* (12), 3116-3136. DOI: 10.1016/j.joule.2021.11.001.
(21) Lennartson, A.; Roffey, A.; Moth-Poulsen, K. Designing photoswitches for molecular solar thermal energy storage. *Tetrahedron Lett.* **2015**, *56* (12), 1457-1465. DOI: 10.1016/j.tetlet.2015.01.187.
(22) Kolpak, A. M.; Grossman, J. C. Azobenzene-functionalized carbon nanotubes as high-energy density solar thermal fuels. *Nano Lett* **2011**, *11* (8), 3156-3162. DOI: 10.1021/nl201357n.
(23) Wang, Z.; Losantos, R.; Sampedro, D.; Morikawa, M.-a.; Börjesson, K.; Kimizuka, N.; Moth-Poulsen, K. Demonstration of an azobenzene derivative based solar thermal energy storage system. *Journal of Materials Chemistry A* **2019**, *7* (25), 15042-15047. DOI: 10.1039/c9ta04905c.
(24) Wu, S.; Butt, H. J. Solar-Thermal Energy Conversion and Storage Using Photoresponsive Azobenzene-Containing Polymers. *Macromol Rapid Commun* **2020**, *41* (1), e1900413. DOI: 10.1002/marc.201900413.
(25) Jones, G.; Reinhardt, T. E.; Bergmark, W. R. Photon energy storage in organic materials—The case of linked anthracenes. *Solar Energy* **1978**, *20* (3), 241-248. DOI: 10.1016/0038-092x(78)90103-2.
(26) Ganguly, G.; Sultana, M.; Paul, A. Designing Efficient Solar-Thermal Fuels with [n.n](9,10)Anthracene Cyclophanes: A Theoretical Perspective. *J. Phys. Chem. Lett.* **2018**, *9* (2), 328-334. DOI: 10.1021/acs.jpclett.7b03170.
(27) Börjesson, K.; Lennartson, A.; Moth-Poulsen, K. Fluorinated fulvalene ruthenium compound for molecular solar thermal applications. *Journal of Fluorine Chemistry* **2014**, *161*, 24-28. DOI: 10.1016/j.jfluchem.2014.01.012.
(28) Boese, R.; Cammack, J. K.; Matzger, A. J.; Pflug, K.; Tolman, W. B.; Vollhardt, K. P. C.; Weidman, T. W. Photochemistry of (Fulvalene)tetracarbonyldiruthenium and Its Derivatives: Efficient Light Energy Storage Devices. *J. Am. Chem. Soc.* **1997**, *119* (29), 6757-6773. DOI: 10.1021/ja9707062.

(29) Moth-Poulsen, K.; Ćoso, D.; Börjesson, K.; Vinokurov, N.; Meier, S. K.; Majumdar, A.; Vollhardt, K. P. C.; Segalman, R. A. Molecular solar thermal (MOST) energy storage and release system. *Energy & Environmental Science* **2012**, *5* (9). DOI: 10.1039/c2ee22426g.
(30) Borjesson, K.; Coso, D.; Gray, V.; Grossman, J. C.; Guan, J.; Harris, C. B.; Hertkorn, N.; Hou, Z.; Kanai, Y.; Lee, D.; et al. Exploring the potential of fulvalene dimetals as platforms for molecular solar thermal energy storage: computations, syntheses, structures, kinetics, and catalysis. *Chemistry* **2014**, *20* (47), 15587-15604. DOI: 10.1002/chem.201404170.
(31) Vlasceanu, A.; Koerstz, M.; Skov, A. B.; Mikkelsen, K. V.; Nielsen, M. B. Multistate Photoswitches: Macrocyclic Dihydroazulene/Azobenzene Conjugates. *Angewandte Chemie* **2018**, *130* (21), 6177-6180. DOI: 10.1002/ange.201712942.
(32) Skov, A. B.; Petersen, J. F.; Elm, J.; Frandsen, B. N.; Santella, M.; Kilde, M. D.; Kjaergaard, H. G.; Mikkelsen, K. V.; Nielsen, M. B. Towards Storage of Solar Energy in Photochromic Molecules: Benzannulation of the Dihydroazulene/Vinylheptafulvene Couple. *ChemPhotoChem* **2017**, *1* (5), 206-212. DOI: 10.1002/cptc.201600046.
(33) Mogensen, J.; Christensen, O.; Kilde, M. D.; Abildgaard, M.; Metz, L.; Kadziola, A.; Jevric, M.; Mikkelsen, K. V.; Nielsen, M. B. Molecular Solar Thermal Energy Storage Systems with Long Discharge Times Based on the Dihydroazulene/Vinylheptafulvene Couple. *Eur. J. Org. Chem.* **2019**, *2019* (10), 1986-1993. DOI: 10.1002/ejoc.201801776.
(34) Kilde, M. D.; Arroyo, P. G.; Gertsen, A. S.; Mikkelsen, K. V.; Nielsen, M. B. Molecular solar thermal systems - control of light harvesting and energy storage by protonation/deprotonation. *RSC Adv* **2018**, *8* (12), 6356-6364. DOI: 10.1039/c7ra13762a.
(35) Hillers-Bendtsen, A. E.; Quant, M.; Moth-Poulsen, K.; Mikkelsen, K. V. Investigation of the Structural and Thermochemical Properties of [2.2.2]-Bicyclooctadiene Photoswitches. *J. Phys. Chem. A* **2021**, *125* (48), 10330-10339. DOI: 10.1021/acs.jpca.1c07737.
(36) Quant, M.; Hillers-Bendtsen, A. E.; Ghasemi, S.; Erdelyi, M.; Wang, Z.; Muhammad, L. M.; Kann, N.; Mikkelsen, K. V.; Moth-Poulsen, K. Synthesis, characterization and computational evaluation of bicyclooctadienes towards molecular solar thermal energy storage. *Chem Sci* **2022**, *13* (3), 834-841. DOI: 10.1039/d1sc05791j.
(37) Manso, M.; Tebikachew, B. E.; Moth-Poulsen, K.; Nielsen, M. B. Heteroaryl-linked norbornadiene dimers with redshifted absorptions. *Org Biomol Chem* **2018**, *16* (31), 5585-5590. DOI: 10.1039/c8ob01470a.
(38) Manso, M.; Fernandez, L.; Wang, Z.; Moth-Poulsen, K.; Nielsen, M. B. Donor-Acceptor Substituted Benzo-, Naphtho- and Phenanthro-Fused Norbornadienes. *Molecules* **2020**, *25* (2). DOI: 10.3390/molecules25020322.
(39) Jevric, M.; Petersen, A. U.; Manso, M.; Kumar Singh, S.; Wang, Z.; Dreos, A.; Sumby, C.; Nielsen, M. B.; Borjesson, K.; Erhart, P.; et al. Norbornadiene-Based Photoswitches with Exceptional Combination of Solar Spectrum Match and Long-Term Energy Storage. *Chemistry* **2018**, *24* (49), 12767-12772. DOI: 10.1002/chem.201802932.
(40) Wang, Z.; Roffey, A.; Losantos, R.; Lennartson, A.; Jevric, M.; Petersen, A. U.; Quant, M.; Dreos, A.; Wen, X.; Sampedro, D.; et al. Macroscopic heat release in a molecular solar thermal energy storage system. *Energy & Environmental Science* **2019**, *12* (1), 187-193. DOI: 10.1039/c8ee01011k.
(41) Orrego-Hernandez, J.; Dreos, A.; Moth-Poulsen, K. Engineering of Norbornadiene/Quadricyclane Photoswitches for Molecular Solar Thermal Energy Storage Applications. *Acc Chem Res* **2020**, *53* (8), 1478-1487. DOI: 10.1021/acs.accounts.0c00235.
(42) Dubonosov, A. D.; Bren, V. A.; Chernoivanov, V. A. Norbornadiene–quadricyclane as an abiotic system for the storage of solar energy. *Russ. Chem. Rev.* **2002**, *71* (11), 917-927. DOI: 10.1070/RC2002v071n11ABEH000745.
(43) Nucci, M.; Marazzi, M.; Frutos, L. M. Mechanochemical Improvement of Norbornadiene-Based Molecular Solar–Thermal Systems Performance. *ACS Sustainable Chemistry & Engineering* **2019**, *7* (24), 19496-19504. DOI: 10.1021/acssuschemeng.9b04503.

(44) Dauben, W. G.; Cargill, R. L. Photochemical transformations—VIII. *Tetrahedron* **1961**, *15* (1-4), 197-201. DOI: 10.1016/0040-4020(61)80026-4.
(45) Cristol, S. J.; Snell, R. L. Bridged Polycyclic Compounds. VI. The Photoisomerization of Bicyclo [2,2,1]hepta-2,5-diene-2,3-dicarboxylic Acid to Quadricyclo [2,2,1,02,6,03,5]heptane-2,3-dicarboxylic Acid1,2. *J. Am. Chem. Soc.* **2002**, *80* (8), 1950-1952. DOI: 10.1021/ja01541a043.
(46) Frey, H. M. 63. The thermal isomerisation of quadricyclene (quadricyclo-[2,2,1,02,6,03,5]heptane). Part I. The gas-phase reaction. *Journal of the Chemical Society (Resumed)* **1964**. DOI: 10.1039/jr9640000365.
(47) Hammond, G. S.; Turro, N. J.; Fischer, A. Photosensitized Cycloaddition Reactions1. *J. Am. Chem. Soc.* **2002**, *83* (22), 4674-4675. DOI: 10.1021/ja01483a051.
(48) Dilling, W. L. Intramolecular Photochemical Cycloaddition of Nonconjugated Olefins. *Chem. Rev.* **2002**, *66* (4), 373-393. DOI: 10.1021/cr60242a002.
(49) Fuß, W.; Pushpa, K. K.; Schmid, W. E.; Trushin, S. A. Ultrafast [2 + 2]-cycloaddition in norbornadiene. *Photochem Photobiol Sci* **2002**, *1* (1), 60-66. DOI: 10.1039/b107442c.
(50) Miki, S.; Asako, Y.; Yoshida, Z.-i. Photochromic Solid Films Prepared by Doping with Donor–Acceptor Norbornadienes. *Chemistry Letters* **1987**, *16* (1), 195-198. DOI: 10.1246/cl.1987.195.
(51) Dreos, A.; Wang, Z.; Udmark, J.; Ström, A.; Erhart, P.; Börjesson, K.; Nielsen, M. B.; Moth-Poulsen, K. Liquid Norbornadiene Photoswitches for Solar Energy Storage. *Adv. Energy Mater.* **2018**, *8* (18). DOI: 10.1002/aenm.201703401.
(52) Quant, M.; Lennartson, A.; Dreos, A.; Kuisma, M.; Erhart, P.; Borjesson, K.; Moth-Poulsen, K. Low Molecular Weight Norbornadiene Derivatives for Molecular Solar-Thermal Energy Storage. *Chemistry* **2016**, *22* (37), 13265-13274. DOI: 10.1002/chem.201602530.
(53) Manso, M.; Kilde, M. D.; Singh, S. K.; Erhart, P.; Moth-Poulsen, K.; Nielsen, M. B. Dithiafulvene derivatized donor-acceptor norbornadienes with redshifted absorption. *Phys. Chem. Chem. Phys.* **2019**, *21* (6), 3092-3097. DOI: 10.1039/c8cp07744d.
(54) Gray, V.; Lennartson, A.; Ratanalert, P.; Borjesson, K.; Moth-Poulsen, K. Diaryl-substituted norbornadienes with red-shifted absorption for molecular solar thermal energy storage. *Chem Commun (Camb)* **2014**, *50* (40), 5330-5332. DOI: 10.1039/c3cc47517d.
(55) Elholm, J. L.; Hillers-Bendtsen, A. E.; Hölzel, H.; Moth-Poulsen, K.; Mikkelsen, K. V. High Throughput Screening of Norbornadiene/Quadricyclane Derivates for Molecular Solar Thermal Energy Storage. *Physical Chemistry Chemical Physics* **2022**. DOI: 10.1039/d2cp03032b.
(56) Ree, N.; Koerstz, M.; Mikkelsen, K. V.; Jensen, J. H. Virtual screening of norbornadiene-based molecular solar thermal energy storage systems using a genetic algorithm. *J. Chem. Phys.* **2021**, *155* (18), 184105. DOI: 10.1063/5.0063694.
(57) Roos, B. O.; Merchan, M.; McDiarmid, R.; Xing, X. Theoretical and Experimental Determination of the Electronic Spectrum of Norbornadiene. *J. Am. Chem. Soc.* **2002**, *116* (13), 5927-5936. DOI: 10.1021/ja00092a049.
(58) Xing, X.; Gedanken, A.; Sheybani, A.-H.; McDiarmid, R. The 198-225-nm Transition of Norbornadiene. *J. Phys. Chem.* **2002**, *98* (34), 8302-8309. DOI: 10.1021/j100085a007.
(59) Antol, I. Photodeactivation paths in norbornadiene. *J. Comput. Chem.* **2013**, *34* (17), 1439-1445. DOI: 10.1002/jcc.23270.
(60) Valentini, A.; van den Wildenberg, S.; Remacle, F. Selective bond formation triggered by short optical pulses: quantum dynamics of a four-center ring closure. *Phys. Chem. Chem. Phys.* **2020**, *22* (39), 22302-22313. DOI: 10.1039/d0cp03435e.
(61) Jorner, K.; Dreos, A.; Emanuelsson, R.; El Bakouri, O.; Fdez. Galván, I.; Börjesson, K.; Feixas, F.; Lindh, R.; Zietz, B.; Moth-Poulsen, K.; et al. Unraveling factors leading to efficient norbornadiene–quadricyclane molecular solar-thermal energy storage systems. *Journal of Materials Chemistry A* **2017**, *5* (24), 12369-12378. DOI: 10.1039/c7ta04259k.

(62) Kuisma, M. J.; Lundin, A. M.; Moth-Poulsen, K.; Hyldgaard, P.; Erhart, P. Comparative Ab-Initio Study of Substituted Norbornadiene-Quadricyclane Compounds for Solar Thermal Storage. *J Phys Chem C Nanomater Interfaces* **2016**, *120* (7), 3635-3645. DOI: 10.1021/acs.jpcc.5b11489.
(63) Chai, J. D.; Head-Gordon, M. Systematic optimization of long-range corrected hybrid density functionals. *J. Chem. Phys.* **2008**, *128* (8), 084106. DOI: 10.1063/1.2834918.
(64) Stanton, J. F.; Bartlett, R. J. The equation of motion coupled-cluster method. A systematic biorthogonal approach to molecular excitation energies, transition probabilities, and excited state properties. *J. Chem. Phys.* **1993**, *98* (9), 7029-7039. DOI: 10.1063/1.464746.
(65) Kendall, R. A.; Dunning, T. H.; Harrison, R. J. Electron affinities of the first-row atoms revisited. Systematic basis sets and wave functions. *J. Chem. Phys.* **1992**, *96* (9), 6796-6806. DOI: 10.1063/1.462569.
(66) Pierloot, K.; Dumez, B.; Widmark, P.-O.; Roos, B. r. O. Density matrix averaged atomic natural orbital (ANO) basis sets for correlated molecular wave functions. *Theor. Chim. Acta* **1995**, *90* (2-3), 87-114. DOI: 10.1007/bf01113842.
(67) Pou-Amérigo, R.; Merchán, M.; Nebot-Gil, I.; Widmark, P.-O.; Roos, B. O. Density matrix averaged atomic natural orbital (ANO) basis sets for correlated molecular wave functions. *Theor. Chim. Acta* **1995**, *92* (3), 149-181. DOI: 10.1007/bf01114922.
(68) Widmark, P.-O.; Malmqvist, P.-k.; Roos, B. r. O. Density matrix averaged atomic natural orbital (ANO) basis sets for correlated molecular wave functions. *Theor. Chim. Acta* **1990**, *77* (5), 291-306. DOI: 10.1007/bf01120130.
(69) Widmark, P.-O.; Persson, B. J.; Roos, B. r. O. Density matrix averaged atomic natural orbital (ANO) basis sets for correlated molecular wave functions. *Theor. Chim. Acta* **1991**, *79* (6), 419-432. DOI: 10.1007/bf01112569.
(70) Plasser, F.; Mewes, S. A.; Dreuw, A.; Gonzalez, L. Detailed Wave Function Analysis for Multireference Methods: Implementation in the Molcas Program Package and Applications to Tetracene. *J. Chem. Theory Comput.* **2017**, *13* (11), 5343-5353. DOI: 10.1021/acs.jctc.7b00718.
(71) Fdez Galvan, I.; Vacher, M.; Alavi, A.; Angeli, C.; Aquilante, F.; Autschbach, J.; Bao, J. J.; Bokarev, S. I.; Bogdanov, N. A.; Carlson, R. K.; et al. OpenMolcas: From Source Code to Insight. *J. Chem. Theory Comput.* **2019**, *15* (11), 5925-5964. DOI: 10.1021/acs.jctc.9b00532.
(72) Neese, F. The ORCA program system. *Wiley Interdiscip. Rev. Comput. Mol. Sci.* **2012**, *2* (1), 73-78. DOI: 10.1002/wcms.81.
(73) Li, J.; Reiser, P.; Boswell, B. R.; Eberhard, A.; Burns, N. Z.; Friederich, P.; Lopez, S. A. Automatic discovery of photoisomerization mechanisms with nanosecond machine learning photodynamics simulations. *Chem. Sci.* **2021**, *12* (14), 5302-5314. DOI: 10.1039/d0sc05610c.
(74) Tully, J. C. Molecular dynamics with electronic transitions. *J. Chem. Phys.* **1990**, *93* (2), 1061-1071. DOI: 10.1063/1.459170.
(75) Barbatti, M. Nonadiabatic dynamics with trajectory surface hopping method. *Wiley Interdiscip. Rev. Comput. Mol. Sci.* **2011**, *1* (4), 620-633. DOI: 10.1002/wcms.64.
(76) Pittner, J.; Lischka, H.; Barbatti, M. Optimization of mixed quantum-classical dynamics: Time-derivative coupling terms and selected couplings. *Chem. Phys.* **2009**, *356* (1-3), 147-152. DOI: 10.1016/j.chemphys.2008.10.013.
(77) Granucci, G.; Persico, M. Critical appraisal of the fewest switches algorithm for surface hopping. *J. Chem. Phys.* **2007**, *126* (13), 134114. DOI: 10.1063/1.2715585.
(78) Crespo-Otero, R.; Barbatti, M. Spectrum simulation and decomposition with nuclear ensemble: formal derivation and application to benzene, furan and 2-phenylfuran. *Theor. Chem. Acc.* **2012**, *131* (6). DOI: 10.1007/s00214-012-1237-4.
(79) Dahl, J. P.; Springborg, M. The Morse oscillator in position space, momentum space, and phase space. *J. Chem. Phys.* **1988**, *88* (7), 4535-4547. DOI: 10.1063/1.453761.

(80) Li, J.; Lopez, S. A. Excited-State Distortions Promote the Photochemical 4pi-Electrocyclizations of Fluorobenzenes via Machine Learning Accelerated Photodynamics Simulations. *Chemistry* **2022**, e202200651. DOI: 10.1002/chem.202200651.
(81) Ben-Nun, M.; Martínez, T. J. Photodynamics of ethylene: ab initio studies of conical intersections. *Chem. Phys.* **2000**, *259* (2-3), 237-248. DOI: 10.1016/s0301-0104(00)00194-4.
(82) Alex, W.; Lorenz, P.; Henkel, C.; Clark, T.; Hirsch, A.; Guldi, D. M. Solar Energy Storage: Competition between Delocalized Charge Transfer and Localized Excited States in the Norbornadiene to Quadricyclane Photoisomerization. *J. Am. Chem. Soc.* **2022**, *144* (1), 153-162. DOI: 10.1021/jacs.1c04322.

TOC:

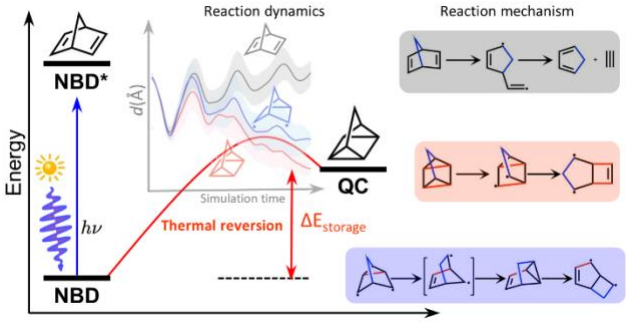

We study the deactivation mechanisms of photoexcited NBD with CASSCF coupled to nonadiabatic dynamics simulation. We follow the excited-state dynamics of NBD that fully traverse the reaction coordinate from the initially excited NBD to product(s).